Heat wave contribution to 2022's extreme glacier melt from automated real-time ice ablation readings

Aaron Cremona[1,2], Matthias Huss[1,2,3], Johannes Marian Landmann[1,2,4], Joël Borner[1,5], and Daniel Farinotti[1,2]

[1]Laboratory of Hydraulics, Hydrology and Glaciology (VAW), ETH Zurich, Zurich, Switzerland
[2]Swiss Federal Institute for Forest, Snow and Landscape Research (WSL), Birmensdorf, Switzerland
[3]Department of Geosciences, University of Fribourg, Fribourg, Switzerland
[4]Federal Office of Meteorology and Climatology, MeteoSwiss, Zurich-Airport, Switzerland
[5]WSL Institute for Snow and Avalanche Research SLF, Davos, Switzerland

Correspondence: Aaron Cremona (cremona@vaw.baug.ethz.ch)

Abstract. Accelerating glacier melt rates were observed during the last decades. Substantial ice loss occurs particularly during heat waves that are expected to intensify in the future. Because measuring and modelling glacier mass balance at the daily scale remains challenging, short-term mass balance variations, including extreme melt events, are poorly captured. Here, we present a novel approach based on computer-vision techniques for automatically determining daily mass balance variations at the local scale. The approach is based on the automated recognition of color-taped ablation stakes from camera images, and is tested and validated at six stations installed on three Alpine glaciers during the summers of 2019-2022. Our approach produces daily mass balance with an uncertainty of $\pm 0.81\,\mathrm{cm\,w.e\,d^{-1}}$, which is about half of the accuracy obtained from ~~manual~~ visual read outs. The automatically retrieved daily mass balances at the six sites were compared to average daily mass balances over the last decade derived from seasonal in situ observations to detect and assess extreme melt events. This allows analyzing the impact that the summer heat waves which occurred in 2022 had on glacier melt. Our results indicate 23 days with extreme melt, showing a strong correspondence between the heat wave periods and extreme melt events. The combination of below-average winter snow fall and a suite of summer heat waves led to unprecedented glacier mass loss. The Swiss-wide glacier storage change during the 25 days of heat waves in 2022 is estimated as $1.27 \pm 0.10\,\mathrm{km^3}$ of water, corresponding to 35% of the overall glacier mass loss during that summer. ~~Compared to the average course of the past decade, the~~ The same 25 days of heat waves ~~in 2022~~ caused a glacier mass loss that corresponds to 56% of the ~~overall~~ average mass loss experienced ~~on average during~~ over the entire melt season during the summers 2010-2020, demonstrating the relevance of heat waves for seasonal melt.

1 Introduction

The prominent and accelerating shrinkage of glaciers worldwide driven by climate change is widely documented (Church et al., 2001; Zemp et al., 2019; Hugonnet et al., 2021). The projected glacier loss will impact sea-level rise (Parkes and Marzeion, 2018; Marzeion et al., 2020), water resources (Immerzeel et al., 2020), and cryosphere-related hazards (Stoffel and Huggel, 2012). In the Alps, the substantial losses with glacier mass balances of about -1 m.w.e. a^{-1} (Huss, 2012; Davaze et al., 2020) have a significant influence on the runoff regime (Farinotti et al., 2016; Huss and Hock, 2018), thus impacting water supply (Immerzeel et al., 2010) and hydropower production (Patro et al., 2018; Schaefli et al., 2019)). Glacier mass balance directly reflects fluctuations in climatic forcing (Ohmura et al., 2007), drives ice dynamics, and determines runoff generation, making it a primary indicator for glacier and climate monitoring (Zemp et al., 2015; Trewin et al., 2021). ~~Despite~~ Although glacier mass balance has been studied extensively with remote sensing (Bamber and Rivera, 2007), in-situ observations (Zemp et al., 2009), and modelling approaches (Hock, 2005; Hock et al., 2019), daily-scale mass balance variations remain mostly unexplored.

Glacier mass balance at the scale of entire glaciers and mountain ranges is often derived from remote sensing products via the geodetic method (Dussaillant et al., 2018; Denzinger et al., 2021; Hugonnet et al., 2021). In it, ice volume change is obtained by differentiating two digital elevation models (DEMs) and translated to mass change by assuming a given density for the volume change (Huss, 2013). ~~However, there are some requirements to be met when calculating the geodetic mass balance, one of these being that the two DEMs should be several years apart (Huss, 2013). Hence, this method is not suitable to assess~~ Interpreting geodetic mass balances at short time scales can be challenging, though, since the results are sensibly affected by the choice of the volume-to-mass conversion factor (Huss, 2013). Recent studies have nevertheless been using results from geodetic studies to gain insights on short-term mass balance variations (e.g. Klug et al., 2018; Vincent et al., 2021; Beraud et al., 2022; Zeller et al., 2022).

Glacier-wide seasonal and annual mass balances are routinely computed from point measurements (Ostrem and Stanley, 1969; Zemp et al., 2009, 2013; Carturan et al., 2016; Sold et al., 2016; O'Neel et al., 2019). The direct glaciological method allows for deriving accumulation and ablation components with ablation stakes, snow probes, and snow pits distributed over the glacier (Ostrem and Stanley, 1969; Dyurgerov et al., 2002; Geibel et al., 2022). Glacier-wide mass balance is then calculated by interpolating the point balances of the network over the entire surface. Methods to do so range from a simple elevation dependence, over hand-drawn contours of equal mass balance, to more advanced statistical methods such as kriging and distributed modelling constrained with local measurements (Dyurgerov et al., 2002; Cogley et al., 2010). Even though glacier-wide mass balance is not directly measured, it is able to capture the temporal variability of glacier mass balance (Fountain and Vecchia, 1999; Thibert et al., 2018). Several studies investigated the temporal variability of mass balance on seasonal to monthly basis, relying on both measurements and ~~modeling~~ modelling (Braithwaite, 1995; Pellicciotti et al., 2005; Huss and Bauder, 2009; Azam et al., 2014; Sold et al., 2016; Mölg et al., 2017). However, models are calibrated on observations, therefore the temporal resolution of these approaches is often limited by the low frequency of measurements.

Recently, techniques to measure mass balance at higher temporal resolution have emerged. Automatic weather station were employed to measure the components of the energy budget and, thus, model the glacier surface energy balance at sub-daily

resolution (Cullen et al., 2007; Fitzpatrick et al., 2017). Gugerli et al. (2019) presented a method for continuous snow water equivalent observations on a glacier surface during winter, relying on a cosmic ray sensor. Automated ablation stakes were developed too. A2PS contributors (2021) presented a station deployed on the glacier surface with a steel wire anchored several

55 ~~meter~~ meters below the ice surface. As the surface melts, the station lowers, the wire is coiled by the station, and the vertical displacement is derived. A different approach was implemented by Landmann et al. (2021) who installed automated cameras monitoring color-coded ablation stakes with a temporal resolution of 20 minutes. From the image time series, the daily melt was derived.

Because these novel methods ~~allows~~ allow measuring mass balance at high temporal resolution, they provide new observation-
60 based insights into short-term mass balance variations, including extreme melt events. In this study, we present an approach for the automated reading of the color-coded ablation stakes ~~proposed by Landmann et al. (2021), which~~ that were presented by Landmann et al. (2021). Our approach allows deriving daily point mass balances automatically via the direct glaciolog-ical method ~~. We developed an algorithm that takes an image time series depicting the stake during the season, acquired at 20-minute intervals, and provides the daily surface mass balances~~ from a time series of close-range images depicting a given
65 ablation stake. The method is tested during the summers of 2019-2021 for six stations installed on three Swiss glaciers. The performance of the algorithm is validated against (i) visual readings of the image time series, and (ii) in-situ measurements. Automatically-derived daily mass balances at the six sites are compared with average daily mass balances over the last decade derived from seasonal in situ observations and modelling to detect and assess extreme melt events. Extreme melt events that occurred during the summer of 2022 are investigated in more detail to evaluate the significance of heat waves for seasonal ice
70 ablation and water runoff. Finally, we discuss the suitability of the method for the detection of extreme glacier melt events at the scale of the Swiss Alps based on point measurements.

2 Study ~~site~~ sites and field data

The three test sites, i.e. Findelgletscher, Glacier de la Plaine Morte, and Rhonegletscher, are medium-sized to large Alpine glaciers located in the central and in the southwestern part of Switzerland (Fig. 1, Table 1). The three glaciers are part of the
75 long-term monitoring program GLAMOS (Glacier Monitoring Switzerland). The seasonal and annual mass balances are de-rived via the glaciological method, exploiting a network of 5 to 12 ablation stakes distributed over the glaciers' entire elevation range. In 2019, six autonomous stations equipped with a camera observing an ablation stake were installed on these glaciers in order to monitor local mass balance at a daily basis: FIN 1 (2551 m.a.s.l.) and FIN 2 (3015 m.a.s.l.) on Findelgletscher, PLM (2689 m.a.s.l.) on Glacier de la Plaine Morte, and RHO 1 (2241 m.a.s.l.), RHO 2 (2392 m.a.s.l.) and RHO 3 (2589 m.a.s.l.) on
80 Rhonegletscher (Fig. 1, Table 1). The station setup consists of a camera and an ~~aluminium~~ aluminum stake that is marked with tapes of different colors~~, placed at 2-centimeter intervals~~. The tapes have a width of 2 cm and are placed 2 cm apart (Fig. 2). The only static element of the system is the stake, which is drilled into the ice. The camera construction, instead, is placed at the glacier surface and slides along the fixed stake. The station setup thus uses the camera as a reference point. When observing the images acquired every 20 minutes during the ablation period, it thus appears that the stake is emerging from the ice. To
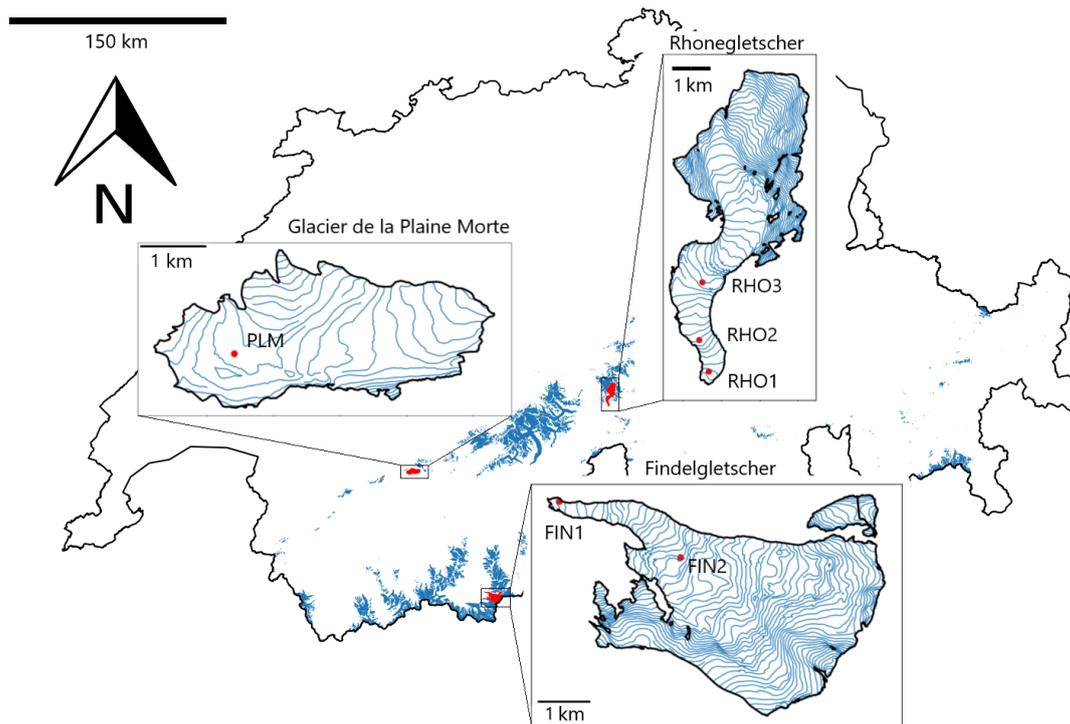
Figure 1. Study site overview. The locations of the six stations installed on Glacier de la Plaine Morte (station PLM), Rhonegletscher (stations RHO 1, RHO 2, and RHO 3), and Findelgletscher (stations FIN 1 and FIN 2) are indicated. Glacier outlines refer to the Swiss Glacier Inventory 2016 (Linsbauer et al., 2021), whereas region boundaries and contour lines are provided by swisstopo.

Table 1. Glacier and station characteristics. Area and elevation refer to the year 2019 (GLAMOS, 2021).

	Area (km^2)	Elevation range (m a.s.l)	Camera stations		
Findelgletscher	12.7	2561-3937	FIN 1 (2551 m a.s.l)	FIN 2 (3015 m a.s.l)	
Plaine Morte	7.1	2470-2828	PLM (2689 m a.s.l)		
Rhonegletscher	15.3	2223-3596	RHO 1 (2241 m a.s.l)	RHO 2 (2392 m a.s.l)	RHO 3 (2589 m a.s.l)

85 automatically read the stake, all images acquired during the season are processed with a computer-vision algorithm is used to derive the stake displacement between two images. From this that derives the stake emergence between pairs of subsequent images. Note that the stake emergence is the vertical movement of the stake out of the ice and is not to be confused with the concept of "emergence velocity", i.e. the difference between the local elevation change and mass balance. From the stake emergence, the mass balance is derived. The six stations were operated during the summer seasons of 2019-2022 (see Table 2

90 for the individual operation periods), providing point mass balances at the daily time scale.
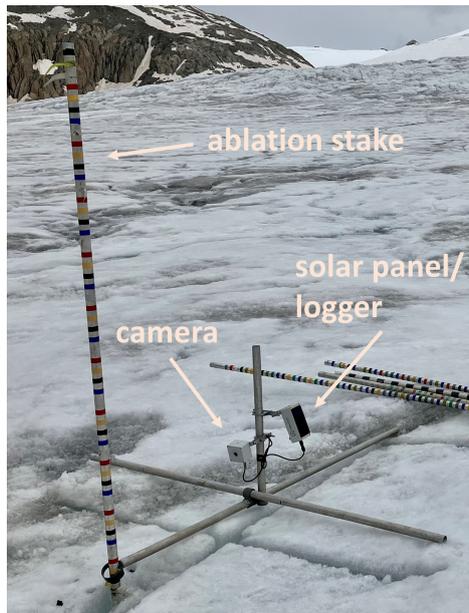
Figure 2. The station setup used to monitor the daily mass balance. The camera acquires pictures of the taped ablation stake every 20 minutes. For details of the setup, refer to Landmann et al. (2021).

Table 2. Operation periods of all stations during the summer seasons 2019-2021.

Year	FIN 2	FIN 1	PLM	RHO 3	RHO 2	RHO 1
2019	27.06-17.09	27.06-17.09	19.06-19.09	26.07-03.10	13.08-03.10	26.07-03.10
2020	16.06-15.09	16.06-15.09	30.06-04.09	24.04-24.09	15.06-24.09	15.06-24.09
2021	08.04-22.09	08.04-22.09	26.06-18.09	21.04-29.09	21.04-29.09	28.06-29.09
2022	not installed	06.04-05.09	04.04-23.09	21.04-24.09	not installed	not installed

3 Methods

3.1 Automated stake reading

We develop an algorithm that exploits computer-vision techniques to automatically derive point mass balance series from a sequence of close-range images of an ablation stake acquired during the melting season. The basis for our algorithm is provided

95 by OpenCV, an open-source library that includes several functions designed to process images and videos (Bradski, 2000). In particular, the framework is built on matchTemplate, a function able to detect objects in an image based on a template of the object to be identified (OpenCV, 2022). The function iteratively compares the template with every portion of the target image, and the correlation between every image portion and the template is returned. A low correlation indicates that the image portion

differs significantly from the template, whereas the higher the correlation, the more similar the two images are. A correlation of 1 indicates perfect agreement and can only be obtained if the template is part of the target image. The matchTemplate function may be employed in two different ways: 1) to detect a single object, and 2) to detect multiple objects. In the first case, the object is detected by simply selecting the pixel with the maximum correlation value. In the second case, every pixel with a correlation above a certain threshold is depicted as a match.

For our application, we want to detect the largest number of tapes that are placed on the stake in every image. Since a tape may look different in two subsequent images (e.g. because of changes in the illumination, caused by different cloud conditions), a relatively low correlation threshold of 0.75 is chosen. The stability of the method is also affected by the choice of template, and a tape stripe with high saturation and favourable illumination has to be preferred.

The choice of a low correlation threshold ~~has also~~ also has some drawbacks. In particular, this can cause other features in the images to be wrongly detected as tapes (Fig. 3). A two-step filtering procedure is therefore applied. The first step consists of removing duplicate matches to avoid redundancy. Such duplicate matches stem from the fact that matchTemplate operates pixelwise, and that many matches are found in the proximity of a tape. Clusters of matches are reduced to single matches according to the highest correlation within the cluster (Fig. 3). The second step consists of a collinearity check. Because all tapes are placed on the stake, i.e. on a linear feature, the correct matches are collinear. Here, we assume that the line intersecting the highest number of matches corresponds to the stake. Matches that do not intersect this line are probably located off the stake, and correspond to features that are wrongly detected and thus filtered out. After this procedure, only collinear and non-redundant matches are preserved, corresponding to the tapes placed on the ablation stake.

An important limitation of matchTemplate is that it is unknown which match in a given image corresponds to which one in the subsequent image. However, most of the superimposed matches that are detected in two consecutive frames (Fig. 4 d) experience a very similar displacement. This is because the tapes lie on the stake, and thus move together, meaning that the displacement must be the same for every tape. Exploiting this property, the difference in position for all possible ~~tape~~ combinations is calculated, and projected onto the stake axis (red line in Fig. 3) with the following equation:

$$d_k = \frac{y_{p,i-1} - y_{q,i}}{\cos \alpha_i}. \tag{1}$$

Here, α is the stake inclination with respect to the vertical axis, i.e. the angle between the red line in Figure 3 and the vertical axis. The inclination is derived automatically by the algorithm. y is the coordinate of a match in the current (i) or previous ($i-1$) image, $q \in [0, m]$ is the number of matches in image i, $p \in [0, n]$ is the number of matches in image $i-1$, and d_k is the displacement between two matches in two consecutive images projected to the stake axis ($k \in [0, (m \cdot n)]$). Finally, the displacement occurring most frequently is taken as the stake ~~displacement~~emergence.

Figure 4 shows this procedure with an example: in Figure 4 a, ten tapes are detected (highlighted in blue), whereas in ~~in~~ Figure 4 b, which is the subsequent camera image, twelve tapes are detected (highlighted in yellow). By calculating the difference of the position between all combinations of tapes, the most frequent displacement, occurring eight times, corresponds to 0.668 pixels (Fig. 4 d). This is taken as stake ~~displacement~~ emergence during the considered time period, and thus, as vertical ice melt.
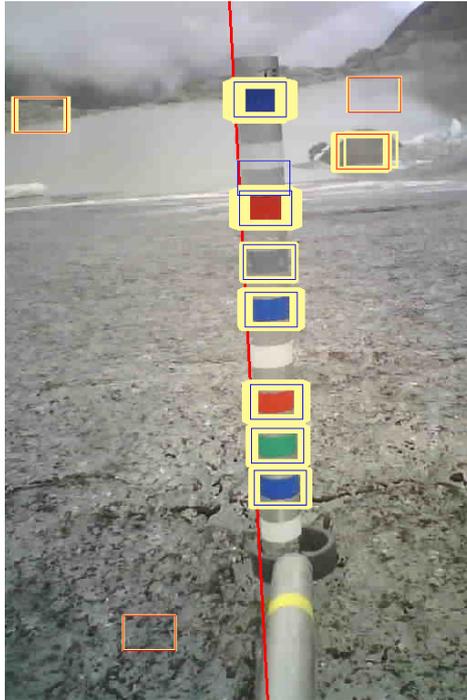
Figure 3. Two-step filtering procedure. (1) Clusters of matches (yellow) are reduced to single matches (red). (2) Non-collinear matches, i.e. not intersecting the red, almost-vertical line, are filtered out. Tapes that are located on the stake are preserved (blue).

The procedure works recursively, meaning that if the stake ~~displacement~~ emergence between the current image (index i) and the previous image (index i-1) cannot be calculated, then images i and i-2 are compared. This can generally be repeated up to 20 times, ~~afterwards~~ afterward which the correlation becomes too low to calculate any ~~displacement~~emergence.

~~Pixel displacements~~ Emergences in pixel units can be transformed into metric units by multiplying them with a conversion factor c according to the following equation:

$$c = \frac{d_{\text{ref,cm}}}{d_{\text{ref,px}}}. \tag{2}$$

Here, $d_{\text{ref,px}}$ is the ~~most frequent~~ average distance between all possible tape combinations in an image, and $d_{\text{ref,cm}} = 4\,\text{cm}$ is the reference distance between two tapes. In the example of Figure 4 a, the average distance between the tapes corresponds to 42.7 px, resulting in a conversion factor of $c = 0.094\,\text{cm}\,\text{px}^{-1}$. This conversion method has the advantage of compensating for distortion errors. In fact, depending on the relative angle between the camera and the stake, the measured distance between two tapes at the top of the stake can differ considerably from the distance between two tapes at the bottom of the stake. The impact of such differences is reduced by taking the average pixel distance. Converting the ~~displacements~~ emergences from pixel to metric units is the last step of the algorithm to derive the stake ~~displacements~~emergences, which is then converted to mass balance with a multiplication with the density of the surface material. For bare ice, a density of $900\,\text{kg}\,\text{m}^{-3}$ is assumed. For snow-covered surfaces, a density of $600\,\text{kg}\,\text{m}^{-3}$ is assumed, which is derived from two snow-density measurements conducted
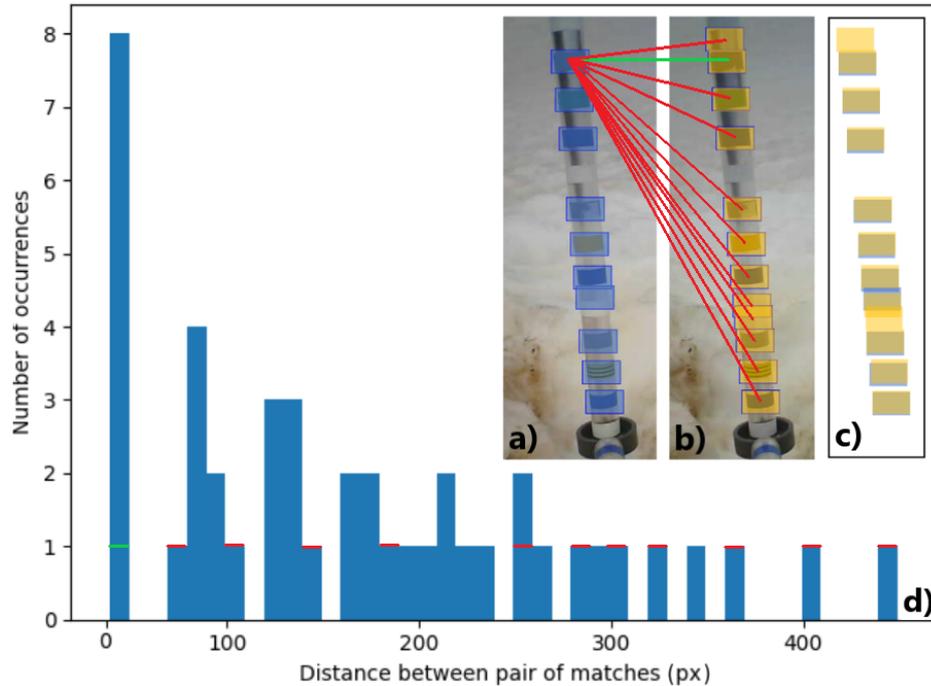
Figure 4. Stake ~~displacement~~ emergence calculation. (a) Filtered matches in image i-1 in blue. (b) Filtered matches in image i in yellow. (c) The two sets of matches are superimposed. (d) Occurrence of displacements d_k resulting from the difference of the positions between all possible combinations of tapes. As an example, the top match in image i-1 (panel a) is compared with all the tapes in image i (panel b). The red lines show combinations of matches that provide displacements that are different than the stake emergence, whereas the green line provides the correct displacement. The displacement of each combination is reported in panel d (green and red horizontal lines). The procedure is repeated for every match in image i, and the most frequent displacement ~~in this case corresponds to~~ (0.668 pixels ~~, which~~ in the example) is taken as stake ~~displacement~~emergence.

on Glacier de la Plaine Morte in June 2019 and 2020, thus accounting for similar snow conditions, i.e. a snowpack during summer ablation (Gugerli et al., 2019). During summer snowfall, the algorithm is not able to capture accumulation ~~,~~because the snow which accumulates on the surface covers the camera but does not cause any relative movement between the camera and the stake~~displacement,~~. The stake emergence is thus equal to zero, ~~is assumed as the ablation~~which is also our ablation reading. An example of application showing the automated ablation reading on Findelgletscher can be found in the video supplement of this article.

3.2 Validation of automated stake reading

The automated stake reading algorithm is tested and validated with the images from the six stations acquired in the summer seasons of 2019-2021. In some cases, we observed a deterioration of the tapes over time. This causes the algorithm to struggle because of lower correlations and the correlation threshold had to be manually adjusted for the algorithm to work properly

(Table 3). For some stake segments with strongly deteriorated tapes, the algorithm was unable to process the entire image time series and stopped along the way. In these cases, i.e. 15% of the readings, the gap was filled with visual readings.

Table 3. Correlation threshold used to process the image time series during the seasons 2019-2022. Stations FIN 2, RHO 2, and RHO 1 were not operated during the summer 2022 and thresholds are therefore not given. For PLM in 2022, the strong degradation of the tapes only enabled visual readings (as opposed to automated ones).

	FIN 2	FIN 1	PLM	RHO 3	RHO 2	RHO 1
2019	0.75	0.75	0.75	0.75	0.75	0.75
2020	0.70	0.75	0.67	0.70	0.75	0.75
2021	0.75	0.70	0.70	0.70	0.70	0.70
2022	-	0.69	-	0.72	-	-

For validation, the ~~results of the automated algorithm~~automated readings (i.e. the outcomes of the algorithm), were compared to (i) visual readings of the same image time series (performed following Landmann et al. (2021)), and (ii) in-situ stake readings ~~. Visual readings of the images are performed following Landmann et al. (2021)~~obtained by following the glaciological method. In-situ stake readings were conducted two to five times per season in conjunction with the installation and maintenance of the stations, as well as with other field campaigns. By comparing the ~~algorithms~~algorithm's outcomes with the visual image readings, the daily errors of the automated approach can be computed. By comparing the ~~algorithms'~~algorithm's outcomes with the in-situ observations, the seasonal mean-absolute deviation (MAD) is derived. The results of this validation are provided in Sect. 4.1.

3.3 Mass balance anomalies and extreme events

The automated method provides point mass balance time series for the six stations. However, the stations are located on different glaciers and at various elevations implying that the time series cannot be directly compared against each other. In order to detect extreme melt events at a larger spatial scale, which is our target, we therefore aim at eliminating the local influences and at extracting a daily anomaly in the melt rates. This anomaly is computed with respect to an average course of the daily mass balance, where the average course refers to a longer temporal baseline. To obtain this, we rely on a combination of (i) local, seasonal mass balance measurements performed in the frame of GLAMOS at, or very close to, all six sites since at least 2010, and (ii) simple mass balance modelling for the period 2010-2020. More specifically, a daily, point-based accumulation and temperature-index melt model (Huss and Bauder, 2009; Huss et al., 2021) driven by nearby meteorological measurements is set up, and constrained in every year to exactly match the observed mass balance at both the date of the April and the September survey. This means that the seasonal mass balance variations are directly provided by the direct measurements, while the daily variations in between the surveys are given by the mass balance model.

Although the stations' locations are very close to the GLAMOS stakes (for which the long-term average mass balance is available), potential biases need to be corrected for. To correct for these potential biases, the average daily mass balance derived

from the GLAMOS stakes during the summer period is adjusted to match the result derived for the automated reading of the camera observations during the respective years (Fig. 5). For example: for the hydrological year 2021 and station RHO 1, summer melt rates based on automated readings are slightly more negative than the ones inferred from combining the seasonal observations at the nearby reference stake and the modelling (Fig. 5 a). To correct for this bias, the daily difference is computed and superimposed on the long-term average daily mass balance curve as follows (see Fig. 5 b for illustration):

$$\dot{b}_{i,j,\text{GLAMOS,corr}} = \dot{b}_{i,j,\text{GLAMOS}} + (\overline{\dot{b}_{j,\text{cam}}} - \overline{\dot{b}_{j,\text{GLAMOS}}}). \tag{3}$$

Here, $\dot{b}_{i,j,\text{GLAMOS}}$ is the melt rate at day i of year j that is derived from GLAMOS' seasonal measurements, $\overline{\dot{b}_{j,\text{cam}}}$ is the average daily melt rate over the summer of year j that is derived from the camera observations, and $\overline{\dot{b}_{j,\text{GLAMOS}}}$ is the average of $\dot{b}_{i,j,\text{GLAMOS}}$ over the summer of year j.
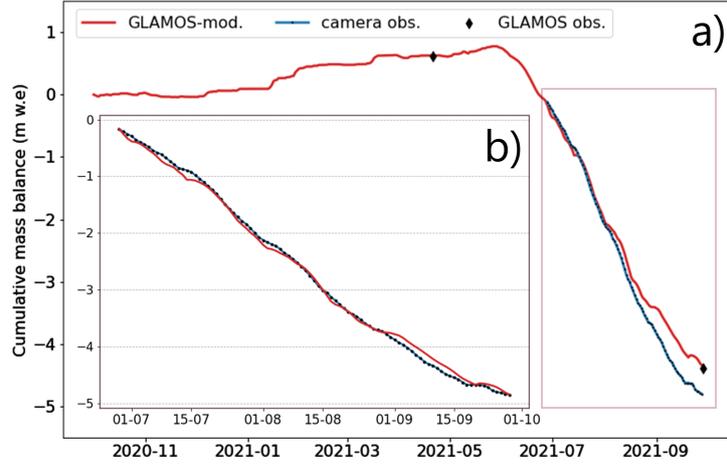
Figure 5. Bias correction for matching the long-term average daily mass balance to the automatically extracted daily ablation. a) Cumulative long-term average daily mass balance based on seasonal observations (black diamonds) combined with modelling (red) and observed daily mass balance at the station (blue). The example refers to RHO 1 during the period 01.10.2020-01.10.2021. Note that the observed daily mass balance is only available during the summer season. (b) Bias-corrected modelled and observed daily mass balances during the period 29.06-29.09.2021.

For each of the four years with camera observations, i.e. 2019-2022, we calculate the average daily difference between the melt rates derived from camera observations and the melt rates derived from seasonal measurements of GLAMOS (Eq. (4)):

$$\Delta\dot{b}_j = \overline{\dot{b}_{j,\text{cam}}} - \overline{\dot{b}_{j,\text{GLAMOS}}} \tag{4}$$

This yields four bias values $\Delta\dot{b}_j$, i.e. one value per year, that are averaged and superimposed on the long-term average daily mass balance (Eq. (5)):

$$\overline{\dot{b}_{i,2010-2020,\text{GLAMOS,corr}}} = \overline{\dot{b}_{i,2010-2020,\text{GLAMOS}}} + \overline{\Delta\dot{b}_j} \tag{5}$$

This procedure ensures correction of the biases resulting from location differences between the stakes of GLAMOS and those used for the automated mass balance reading.

To compare the mass balance signals across the different stations, the daily mass balance anomaly $\Delta\dot{b}_{i,j}$ is calculated for each station (Eq. (6)):

$$\Delta\dot{b}_{i,j} = \dot{b}_{i,j,\text{cam}} - \overline{\dot{b}_{i,2010-2020,\text{GLAMOS},\text{corr}}} \tag{6}$$

The mass balance anomaly is directly comparable across stations, and can be used to define an extreme melt event, i.e. an event in which the anomaly exceeds a certain threshold for all stations. We set this threshold to the 85% quantile of the negative anomalies observed during the years 2019-2021. The year 2022 was omitted when defining the threshold because of the extreme ~~melts~~ melt rates that do not represent the normal conditions. Although in statistical analysis the 97.5% or the 99.5% quantiles are often chosen to define extreme events (Friederichs, 2010; Friederichs et al., 2018), we chose the 85% quantile because we aim at detecting prolonged periods with high melt rates, rather than only a few isolated days with maximal melt. The 85% quantile corresponds to –2.55 cm w.e d^{-1}, and ~~when this threshold is exceeded,~~ the event is classified as extreme ~~.~~ when the mean anomaly across the stations exceeds this threshold. Because the stations have different operation periods (Tab. 2), the mean anomaly may be computed from a different number of stations and consequently be affected. Note that ~~this information~~ the mean mass balance anomaly at the point scale does not directly allow investigation of the influence of the heat waves on glacier melt at the regional scale, and upscaling is therefore needed.

3.4 Upscaling to regional mass balance

To derive the regional, i.e. Swiss-wide, daily glacier mass balance over summer of 2022, we combine the information at the point scale, i.e. the mass balance anomalies derived from the different stations, with information about the regional mass balance. We rely on data sets of glacier-wide seasonal mass balance for 20 glaciers (GLAMOS, 2021), a daily distributed mass balance model for these glaciers (Huss et al., 2021), and multi-decadal ice volume change (Fischer et al., 2015), as well as repeated inventories of surfaces areas for all glaciers (Linsbauer et al., 2021). First, glacier-specific anomalies in glacier-wide mass balance relative to the reference period 2010-2020 are extrapolated to all unmeasured glaciers based on inverse-distance weighting, including a higher weight for observations on the same side of the main Alpine weather divide (North/South). These anomalies are then superimposed on long-term average mass change rates available for every Swiss glacier from Fischer et al. (2015). This yields a series of annual glacier volume and mass changes at the scale of the Swiss Alps (see also Grab et al., 2021). Furthermore, daily time series of glacier-wide mass balance are available for the 20 glaciers with detailed measurements based on a combination of seasonal observations with a distributed mass balance model (Huss et al., 2021; GLAMOS, 2021). We attribute modelled daily mass balance of the closest ~~series~~ of the 20 glaciers with direct mass balance measurements to every glacier of the most recent Swiss glacier inventory (Linsbauer et al., 2021)~~and~~. Subsequently, we match the daily time series to the glacier-specific annual mass balance ~~(see above)~~ as originating from the procedure described above (Grab et al., 2021). This is achieved by equally attributing the misfit between the cumulative daily series and the glacier-specific annual mass

balance to all days of the summer season (June-August). Overall, this procedure provides the average daily course of glacier
mass balance as a mean over the period 2010-2020 for every single glacier.

To calculate the regional-scale mass balance for the summer of 2022, we combine the average regional mass balance 2010-2020 with the mean point mass balance anomaly calculated from the three stations operative in 2022 (Eq. (7)).

$$\dot{B}_{i,2022} = \overline{\dot{B}_{i,2010-2020}} + \Delta\dot{b}_{i,2022}, \tag{7}$$

where i is day of the year, $\dot{B}_{i,2022}$ is the computed regional mass balance for day i of 2022, $\overline{\dot{B}_{i,2010-2020}}$ is the average regional mass balance of period 2010-2020 for day i, and $\Delta\dot{b}_{i,2022}$ is the mean point mass balance anomaly for day i derived from the three stations providing daily measurements. This procedure allows the Swiss-wide glacier mass balance over the summer of 2022 to be estimated at the daily scale. Finally, we compute the Swiss-wide glacier storage change, which accounts for water that is produced from snow- and ice-melt on glacier surfaces over the melt season. The glacier storage change is computed by multiplying the Swiss-wide glacier mass balance with the glacierized area in Switzerland according to the last inventory (2016, Linsbauer et al., 2021).

3.5 Definition of heat waves

To investigate the effect of heat waves on glacier melt at the scale of the Swiss Alps, we follow the definition of Kyselỳ (2002). According to Kyselỳ (2002), heat waves are defined as consecutive periods of at least three days during which the average daily maximum temperature is higher than 30 °C and the daily maximum temperature on individual days does not fall below 25 °C. This second part of the definition allows for hot periods separated by short, minor drops in temperature to be classified as one heat wave. Note that at the meteorological stations that we considered, the maximum daily temperature during the heat waves never lowered below 30 °C, therefore the second part of the definition was not used. The definition of Kyselỳ (2002) considered the temperature at a single station. However, because we are interested to have a representative result at the Swiss-wide scale, we considered the average temperature measured at different sites for defining heat waves. The four sites were chosen to be the meteorological stations in Lugano (273 m a.s.l.), Chur (556 m a.s.l.), Zurich (426 m a.s.l.), and Sion (482 m a.s.l.), because they are scattered over Switzerland and cover a reasonable altitudinal range (in which we can expect temperatures above 30 °C). Hence, we assume the average temperature across the four stations to be representative for the regional scale.

4   Results

4.1   Performance of the automated algorithm

The cumulative mass balance obtained from the automated readings is very consistent with the ~~manual~~ visual readings and the in-situ observations (see example of station RHO 1 in Fig. 6 a-c). The good performance of the algorithm is proven by the boxplots showing the distribution of the daily deviations from the visual readings (Fig. 6 d-f). In 2019, the median daily deviation is 0.06 cm and the mean deviation is –0.01 cm (Fig. 6 d), in 2020, the values are –0.04 cm and –0.11 cm, respectively, and in 2021, they are –0.33 cm and –0.35 cm, respectively (Fig. 6 f). The larger deviations in 2021 are likely a consequence of

the tape degradation over time, which causes the tapes to loose color and to partially detach from the stake. Of note is the fact
that the daily deviations are mostly negative, which might suggest that the automated algorithm ~~overestimate~~ overestimates
melt when compared to the visual readings. However, the comparison of the automatically-retrieved cumulative mass balances
with the reference mass balance (e.g. visual readings and in-situ observations) for all the six sites shows that the algorithm
does not overestimate melt systematically (Fig. 7). With a mean-absolute deviation for the cumulative seasonal melt of 16 cm,

265   Figure 7 shows a good correspondence of the automatically-retrieved mass balances with both the visual readings and in-situ
observations.
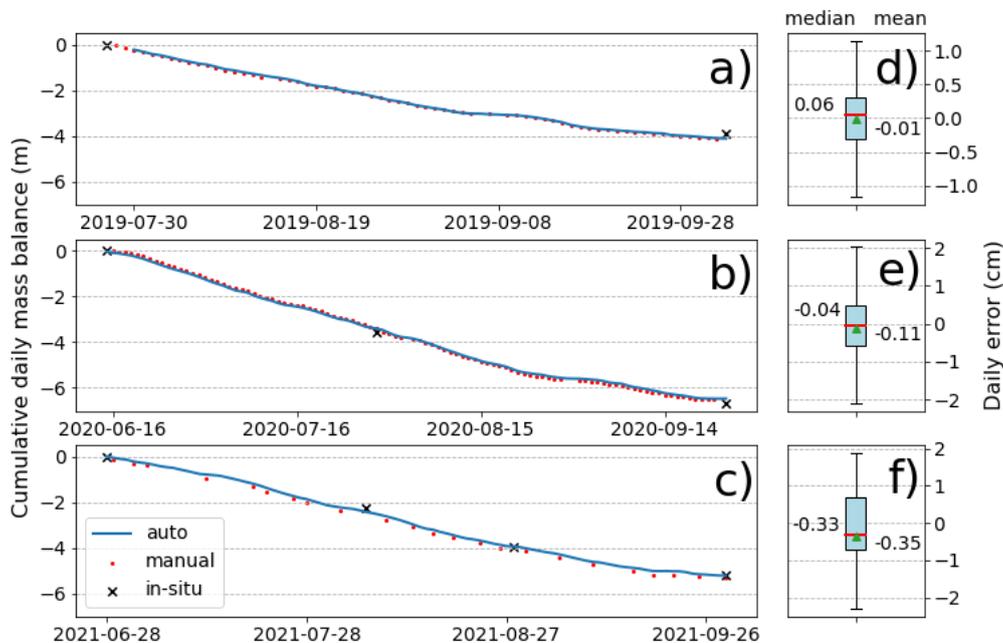
Figure 6. Validation of the automated mass balance readings for the station RHO 1. The cumulative daily mass balance for the years 2019 (a), 2020 (b), and 2021 (c) is shown. The mass balance from the automated method (blue) is validated against visual readings of the images (red) and in-situ observations (black). Panels (d-f) show daily deviations with respect to the visual readings over the seasons 2019, 2020, and 2021, respectively.
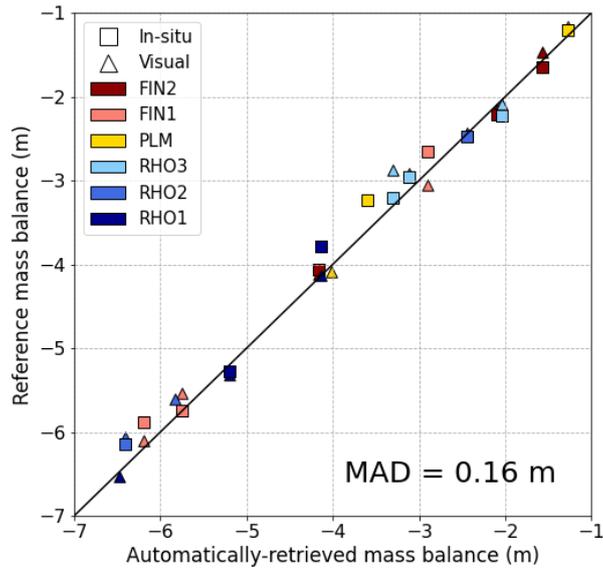
Figure 7. Evaluation of the automatically-retrieved cumulative mass balances against the reference mass balance readings, i.e. visual readings and in-situ observations. Results refer to the six stations installed over the summer seasons of 2019-2021. The seasonal mean-absolute deviation (MAD) is 0.16 m.

4.2 Mass balance anomalies and extreme melt events

To detect and assess extreme melt events, the daily observations obtained with the automated method were compared with the long-term average mass balance, yielding daily mass balance anomalies (Fig. 8). According to our definition (cf. Sect. 3.3), an extreme melt event occurs when the anomaly averaged over all the stations exceeds -2.55 cm w.e d^{-1}.

In 2019, 11 extreme events were identified (Fig. 8 a). They are distributed more or less evenly over the summer and coincide with high air temperatures, as indicated by meteorological records from MeteoSwiss (Meteoswiss, 2020). In 2020, 14 extreme melt events occurred (Fig. 8 b). Similar to the year 2019, the high-melt days are distributed over the entire summer, although in 2020 more events (ca. 50%) are found in August. In 2021, only three extreme melt events occurred (Fig. 8 c). The year was favourable for the glaciers, with only few days with extreme melting in mid-August and with overall melt close to the decadal average. This is very much in contrast to 2022, when 23 events of extreme melt occurred (Fig. 8 d). During most of the summer, the anomalies are very negative, exceeding -1.5 cm w.e d^{-1} for a total of 54 days. In addition, various prolonged periods of high melt occurred throughout the summer. The comparison of the four years evidences that the summer of 2022 saw almost as many extreme melt events as the three previous years combined.
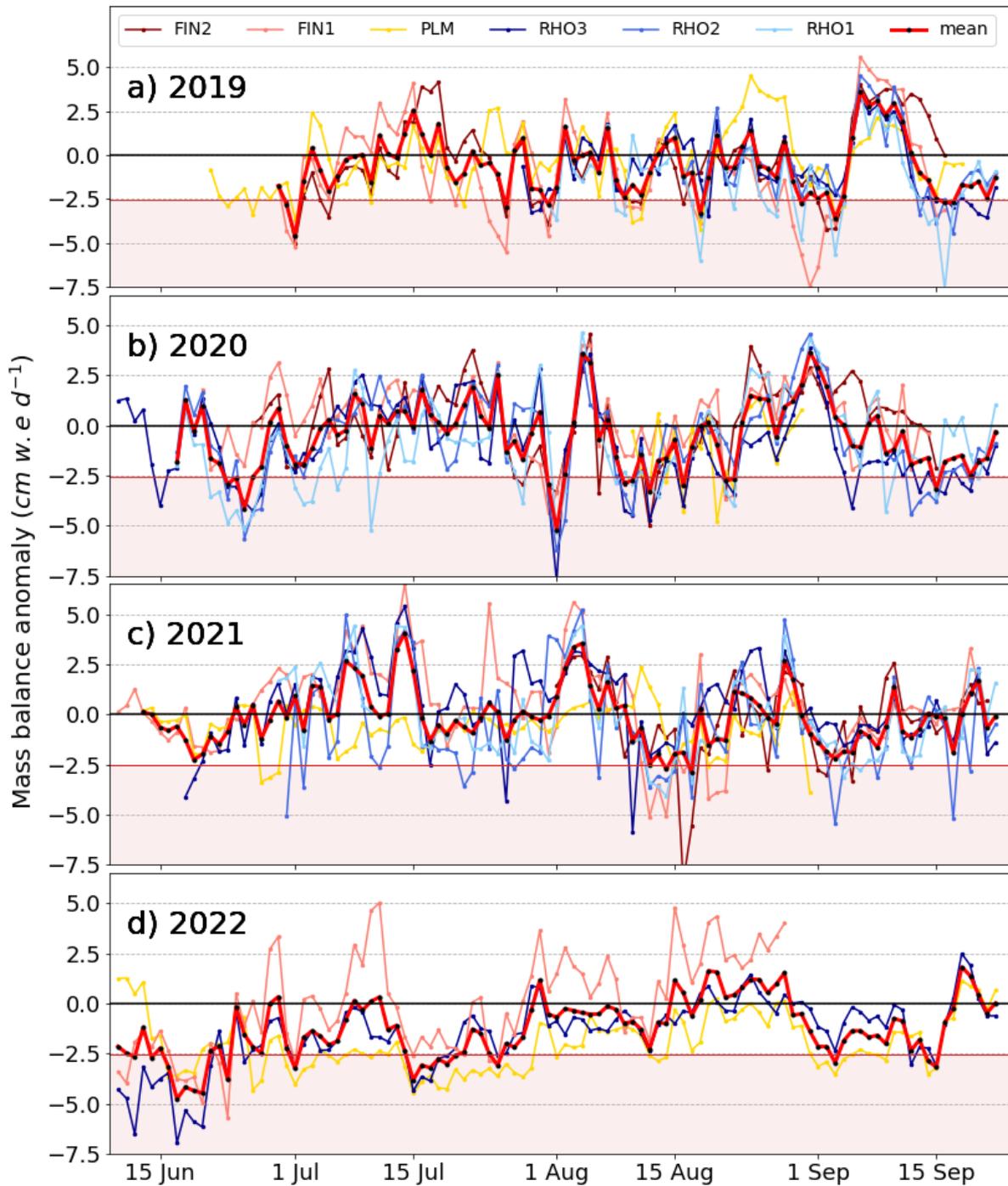
Figure 8. Daily mass balance anomalies for the stations on Findelgletscher (reddish colour), Glacier de la Plaine Morte (yellow), and Rhonegletscher (blueish colour) during the summer seasons of (a) 2019, (b) 2020, (c) 2021, and (d) 2022. The mean anomaly for all stations is shown in red (thick line). With our definition (Sect. 3.3), extreme events occur when the mean anomaly exceeds –2.55 cm w.e d^{-1} (red-shaded area).

4.3 Impact of summer 2022 on Swiss-wide glacier storage change

To further investigate the influence of extreme melt events and the significance of heat waves on the glacier melt in summer 2022, the daily observations were spatially upscaled to estimate the total storage change of all Swiss glaciers (see Sect. 3.4 for methods). ~~For defining heat waves, we follow Hutter et al. (2007), who defined them as consecutive periods of at least three days during which the mean daily maximum temperature is higher than 30 °C. To have a representative result at the Swiss-wide scale, we considered the average temperature measured at four meteorological stations distributed over Switzerland for defining heat waves . The four meteorological stations were chosen to be the ones in Lugano (273 m a. s. l.), Chur (556 m a.s.l.), Zurich (426 m a.s.l.), and Sion (482 m a.s.l.). According to this definition,~~ According to our definition of heat waves (cf. Sect. 3.5), three heat waves occurred during the summer of 2022 for a total of 25 days. The first wave occurred between 17-21 of June, the second between 14-26 of July, and the third between 31 July and 6 August.

Except for August, the Swiss-wide glacier storage change for summer 2022 was significantly higher than the average of the past decade (Fig. 9). Glacier melt was particularly high during the heat waves in June and July, during which 13 out of 23 extreme melt events occurred. During the August heat wave, instead, melting was not particularly extreme. This is because August melt rates were high during the past decade too, meaning that the melt rate anomalies for August 2022 are not exceeding the threshold we use to define extreme melt events.

In addition to the above, Figure 9 shows ten extreme melt events that occur outside of the heat wave periods. These events are at the beginning and at the end of the season, i.e. in June and September, when maximal daily air temperatures remain below 30 °C most of the time and thus do not lead to a heat wave in our definition. The temperatures recorded during June and September 2022 were significantly higher than in June-September of the past decade and ~~were thus able to cause extreme melt , but were not high enough to be also~~ thus caused extreme melt for several days. However, before the first heat wave (which started on 17 June 2022), and during September 2022, the temperatures were never high enough as to be categorized as heat waves.
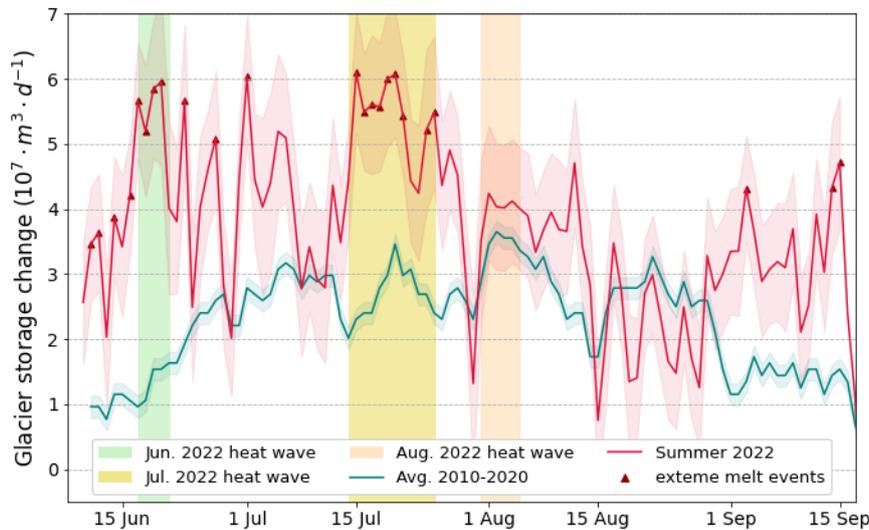
Figure 9. Daily storage change of all ca. 1400 Swiss glaciers. The storage change during summer 2022 (red line) is compared to the average storage change of the past decade (blue line). The red- and blue-shaded areas show the uncertainties, which are calculated as described in Sect. 5.2. Storage change rates occurring during extreme melt events, defined as days with a mass balance anomaly exceeding $-2.55\,\mathrm{cm\,w.e\,d^{-1}}$, are shown by red triangles. The three heat waves that occurred in June, July, and August 2022 are shown in green, yellow, and orange, respectively.

For the period from 10 June to 15 September 2022, we estimate a total storage change for all Swiss glaciers of $3.63 \pm 0.26\,\mathrm{km^3}$ w.e. (cf. Sect. 5.2 for the uncertainty analysis). This is about 60% more than the average storage change of the past decade during the equivalent period ($2.25 \pm 0.10\,\mathrm{km^3}$ w.e.). The annual glacier storage change of 2022 was about three times higher than usual, due to exceptionally low winter accumulation in addition to the high summer ablation (GLAMOS, 2022). During the 25 days of heat waves that occurred in summer 2022, glacier storage change provided $1.27 \pm 0.10\,\mathrm{km^3}$ of water. This corresponds to 35% of the total glacier storage change of summer 2022, and to 56% of the average summer storage change over the past decade. This demonstrates the significance of extreme melt events occurring during heat waves regarding seasonal glacier melt.

5 Discussion

5.1 Spatial correlation of point observations

The approach we use for upscaling the mass balance at the regional scale is simple, and we thus investigate the suitability of using point measurements to detect extreme glacier melt events at the regional scale. To do so, we consider the daily mass balance anomalies across stations and compute their correlation for the summer seasons 2019-2021 (Fig. 10). The daily mass balance anomalies correlate well (r=0.52-0.82, see Fig. 10 a-c) for stations placed on the same glacier, i.e. FIN 1 and FIN 2, as well as RHO 1, RHO 2, and RHO 3. This is in agreement with previous studies showing that glacier mass balance is well

correlated over short to intermediate distances (Lliboutry, 1974; Thibert et al., 2013; Vincent et al., 2017, 2018). The correlation generally decreases between stations that are located on different glaciers. This is expected, since stations on the same glacier are more likely to experience the same meteorological forcing. The correlations between the stations on Findelgletscher and Rhonegletscher range from 0.40-0.74, indicating that albeit weaker agreement, the correlation is preserved. The correlations with the station on Glacier de la Plaine Morte, instead, are generally poor. An exception is given by the year 2020, when the correlation is similar to the one between Findelgletscher and Rhonegletscher. This lower correlation was noticed by Landmann et al. (2021) already, who suggested this to be linked to differences in local meteo-climatic conditions (see also discussion below).
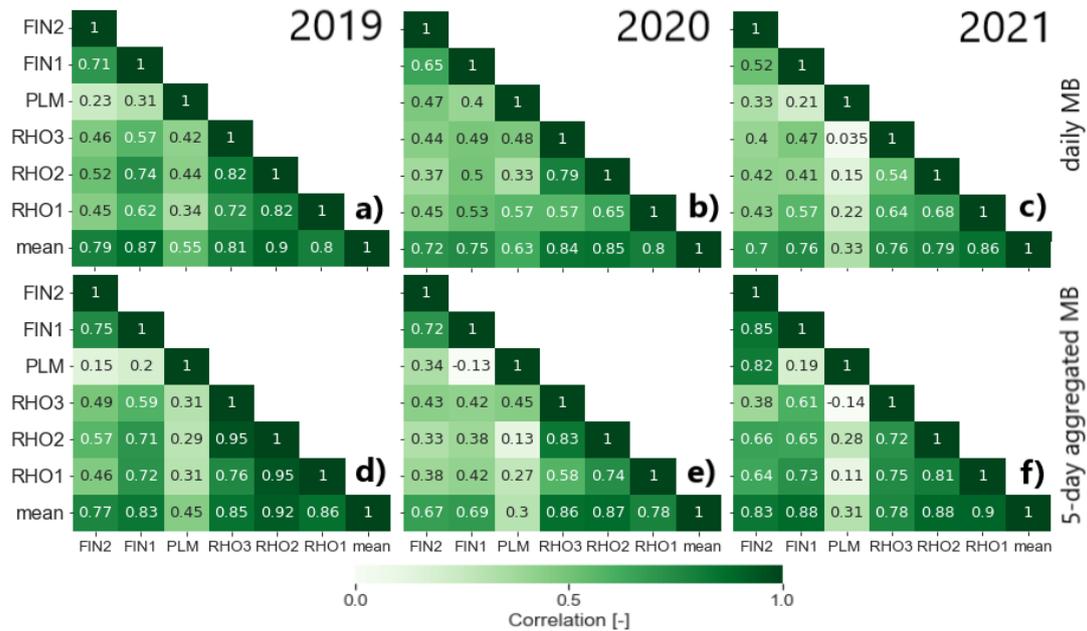
Figure 10. Correlation coefficient (r) of mass balance anomalies between the different stations. a), b), c) show the correlation of the daily mass balance anomalies between the six stations (indicated by their name) and the correlation between each station and the mean of all stations (labelled "mean"). d), e), and f) show the same, but aggregated over a period of five days.

To investigate whether the uncertainties of the algorithm used to automatically extract the daily mass balances have an influence on the correlation between stations, we aggregate the mass balance anomalies to 5-day periods (Fig. 10 d-f). The argument for doing so is that the uncertainty of the daily readings should be independent from each other, meaning that a reading over a longer period of time should have a smaller relative uncertainty and thus increase the correlation. Indeed, the correlations of the so aggregated anomalies increase for stations that are on the same glacier. Similarly, the correlations increase for combinations of stations on Findelgletscher and Rhonegletscher. The anomalies of the stations in Glacier de la Plaine Morte, instead, remain poorly correlated with other stations. The moderate increase in correlation however suggests that the influence of the uncertainties introduced by the automated algorithm are small, thus not affecting our spatial analysis further.

Finally, we computed the correlation between the mean anomaly of all stations and the anomaly at each individual station. This allows assessing whether some stations are more representative than others for the regional-scale signal. The results from both the daily and the 5-days aggregated correlation matrices are congruent (Fig. 10): During the three years with data, the station on Glacier de la Plaine Morte shows a significantly lower correlation with the mean as compared to the other stations. The reason for this is likely to be the different local meteorological forcing: while Findelgletscher and Rhonegletscher are influenced by southerly weather patterns, Glacier de la Plaine Morte experiences weather that is more similar to the Northern flanks of the Alps. This ~~interpretation~~ difference in meteorological forcing is corroborated by major differences in winter snow accumulation at the stations: whereas only 1-2 m of snow are typically present in April on the ~~snout~~ tongue of Findel- and Rhonegletscher, more than 4 m are often recorded on Glacier de la Plaine Morte (Bauder et al., 2020; GLAMOS, 2022). Furthermore, the topographical situation of the station on Glacier de la Plaine Morte differs from the other ones: the station is not located at the tongue of a valley glacier, where catabatic winds influence the surface energy balance, but on a glacier plateau surrounded by mountains that might favour cold air trapping. We conclude that the relatively low number of stations and the fact that they are all located in Southwestern Switzerland is limiting when aiming to infer daily mass balance variability at the regional scale, although we note that the stations are located in the region that holds the most glacier area in the Swiss Alps (Linsbauer et al., 2021).

5.2 Uncertainty analysis

To estimate the overall uncertainty of the regional mass balance of summer 2022, we account for uncertainties stemming from (A) the automated reading algorithm, (B) the modelled daily mass balance for the period 2010-2020, inferred from seasonal observations at GLAMOS stakes, and (C) the average regional mass balance for the period 2010-2020, used for upscaling.

The uncertaintiy of the automated reading algorithm (σ_{alg}) was derived by calculating the mean absolute deviation (MAD) of the automatically-retrieved daily mass balances with respect to the visual readings (Fig. 11 a). The average MAD for the six sites is 0.81 cm w.e d^{-1}. Note that this uncertainty is biased during summer snowfall events due to the large uncertainties of the visual method in such cases. The latter stem from (i) ~~displacements~~ emergences that are very low, and (ii) snow that covers some tapes of the observed stake and the ring at the base of the stake, that serves as reference. This bias is highlighted by the large deviations of the automated readings when visual readings show zero melt (Fig. 11 a). In fact, the algorithm is able to capture smaller ~~displacements~~ emergences than the visual readings, i.e. ~~displacements~~ emergences in the order of a few pixels. Therefore, it appears that the automated method estimates higher ablation for melt rates close to zero, while the visual method fails to capture them. Capturing small ~~displacements~~ emergences also allows measuring melt occurring beneath the fresh snow after summer snowfall events, i.e. when the fresh snow layer is not thick enough to entirely insulate the ice from melt.

Uncertainties of the modelled daily mass balance at the GLAMOS stakes ($\sigma_{\dot{b}}$) were derived by conducting a sensitivity analysis (Fig. 11 b). To investigate the model sensitivity to various inputs, the local daily mass balance model was re-run by still ensuring a match with seasonal observations but by varying (i) the meteorological station providing temperature and precipitation forcing, (ii) the gradient to extrapolate air temperature to the site, and (iii) the ratios between the melt factor and radiation factors of the temperature index model (see Huss and Bauder, 2009). The tested range of all variations is large and

represents what we would consider a maximum offset from the reference setup, i.e. a conservative estimate for the resulting uncertainties. The deviation of the mass balance resulting from the different model runs (e.g. varying inputs (i)-(iii)) from the reference mass balance provides the uncertainties $\sigma_{loc,1}$, $\sigma_{loc,2}$, and $\sigma_{loc,3}$. These uncertainties are considered to be independent and are combined into an overall uncertainty in local mass balance $\sigma_{\dot{b}}$ for every day as

$$\sigma_{\dot{b}} = \sqrt{\sigma_{loc,1}^2 + \sigma_{loc,2}^2 + \sigma_{loc,3}^2},$$

(8)

resulting in daily uncertainties of the modelled point mass balance ranging between 0.19 and 1.18 cm w.e d^{-1} (with a mean value of 0.58 cm w.e d^{-1}).

Uncertainties in the average regional mass balance for the period 2010-2020 were also estimated based on a sensitivity analysis (Fig. 11 c). We recomputed the 2010-2020 regional daily glacier mass balance by (i) varying the set of glaciers featuring daily glacier-wide mass balance variations, (ii) randomly superimposing uncertainties in the observation of the glacier-specific ice volume change (Fischer et al., 2015), and (iii) varying the volume-to-mass conversion factor within ± 60 kg m^{-3}. The deviation of the mass balance resulting from the different model runs (e.g. varying inputs (i)-(iii)) from the reference mass balance provides the uncertainties $\sigma_{reg,1}$, $\sigma_{reg,2}$, and $\sigma_{reg,3}$. Also here, we combine these uncertainties for every day as

$$\sigma_{\dot{B}_{2010-2020}} = \sqrt{\sigma_{reg,1}^2 + \sigma_{reg,2}^2 + \sigma_{reg,3}^2}.$$

(9)

The uncertainty in the daily average mass balance at the scale of all Swiss glaciers $\sigma_{\dot{B}_{2010-2020}}$ is found to range between 0.06 and 0.21 cm w.e d^{-1} (with a mean value of 0.13 cm w.e d^{-1}) with highest values during the summer season.

The uncertainty of the regional mass balance of summer 2022 is then derived by combining the uncertainties of (A) σ_{alg}, (B) $\sigma_{\dot{b}}$, and (C) $\sigma_{\dot{B}_{2010-2020}}$ as

$$\sigma_{\dot{B}_{2022}} = \sqrt{\sigma_{alg}^2 + \sigma_{\dot{b}}^2 + \sigma_{\dot{B}_{2010-2020}}^2}$$

(10)

The mean daily uncertainty of the regional mass balance of summer 2022 $\sigma_{\dot{B}_{2022}}$ is 0.98 cm w.e d^{-1}.

Finally, we derive the uncertainty of the Swiss-wide glacier storage change by propagating the uncertainty of the regional mass balance of summer 2022 ($\sigma_{\dot{B}_{2022}}$) and the uncertainty of the Swiss-wide glacier area (σ_A, Linsbauer et al. (2021)) with

$$\sigma_{dS} = dS \cdot \sqrt{\left(\frac{\sigma_A}{A}\right)^2 + \left(\frac{\sigma_{\dot{B}_{2022}}}{\dot{B}_{2022}}\right)^2}.$$

(11)

The mean daily uncertainty of the Swiss-wide glacier storage change is found to be $\pm 9.8 \cdot 10^6$ m^3 w.e d^{-1}.

Uncertainties of the storage change cumulated over a certain period, i.e. the heat waves and the entire summer, are derived with the same procedure as described in the present section, but first we cumulate the mass balance over the period in question, and then we calculate the corresponding uncertainty assuming all mass balance uncertainties within each period to be independent.
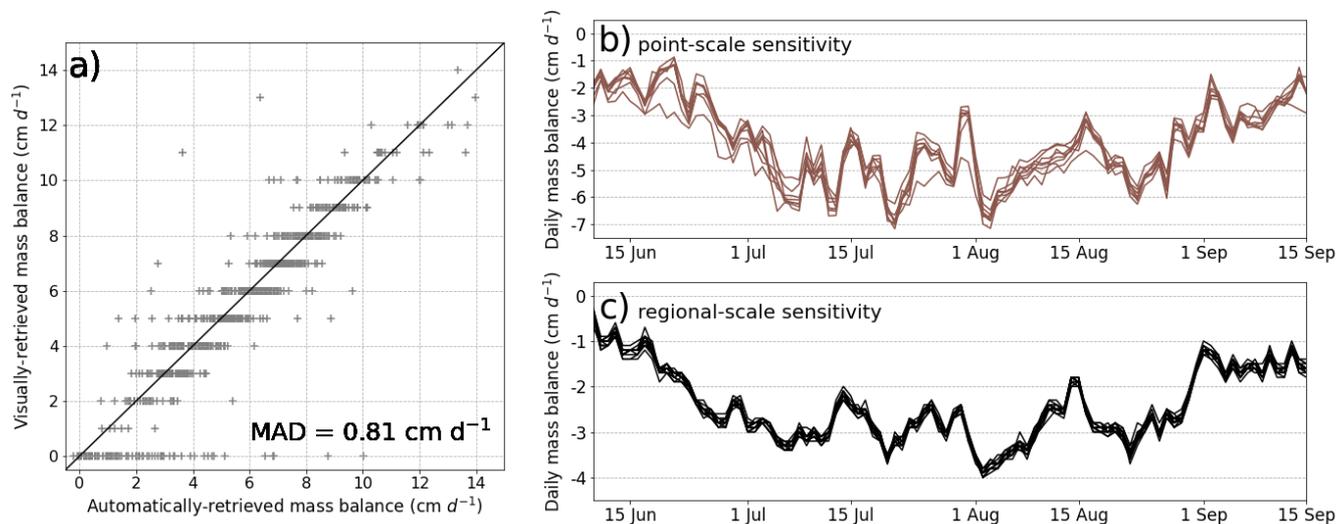
Figure 11. Uncertainty assessment. (a) Evaluation of the automated readings against the visual readings. The resolution of the visual readings is $1\,\mathrm{cm\,w.e\,d^{-1}}$, thus explaining the discrete values on the y-axis. The mean absolute deviation is $0.81\,\mathrm{cm\,w.e\,d^{-1}}$. (b) Sensitivity analysis of the modelled daily mass balance of the last decade for the GLAMOS stake close to station RHO 3. The point-scale model is run with different setups (individual brown lines) to investigate the sensitivity to various inputs. (c) Sensitivity analysis of the average regional mass balance for the period 2010-2020. Similar to (b), the regional-scale model is run with different setups to investigate its sensitivity.

5.3 Limitations and potential of the computer vision algorithm

395 In this section, we discuss the limitations and possible improvements of the computer vision algorithm that we presented. To date, the main limitation of the algorithm is that stake emergences larger than 4 cm between two images cannot be measured. This is because of the ambiguity that is introduced when the tapes move more than a complete phase shift. Indeed, for the algorithm, an emergence of (say) 4 cm looks identical to a phase shift of 8, 12, or 16 cm. This means that the method cannot be applied in cases with ablation > 4 cm between consecutive images (note that this might happen for both cases with higher overall

400 melt rate and cases with images taken with lower temporal resolution). There are two simple solutions for accommodating such cases: 1) place the tapes at larger distances, although this could come at the expense of a less reliable detection, since there would be less tapes visible on every given image, and 2) acquire images with a time interval that is sufficiently low as to prevent stake emergences > 4 cm between two consecutive images. A more elaborate solution would be to adapt the algorithm to use the tapes' color coding, since this would help to resolve the ambiguity. We performed some testing by detecting

405 the color of the tapes, and the tests suggested potential for such an implementation (Cremona et al., 2023). An alternative for solving the problem would be to use a different feature-detection algorithm, such as Scale-Invariant Feature Transform (Lowe, 2004) or Convolutional Neural Networks based methods (Hashemi et al., 2016). Such algorithms might also be able to better deal with both rotations due to stake tilting and scaling of the tapes in the images. The reason that we preferred template matching over such potential alternatives is that the former proved to be very effective in detecting the tapes, even

410 in challenging conditions such as fog (Fig. 12 a, b) or darkness (Fig. 12 c), and when the stake was partially tilted. During the development of the algorithm, we realized that the illumination conditions, as well as the saturation and the color of the tapes, have an important influence on the correct functioning of the template matching procedure. In particular, the proper choice of the template was found to be key for optimal functioning, and tapes with high-contrast and saturated colors were chosen (Borner and Cremona, 2020). On the contrary, tapes with low contrast and saturation (e.g. white and grey) are difficult

415 to detect, leading to the recommendation of always using saturated, high-contrast colors (e.g. red, blue, yellow, and green). The color choice thus represents a trade-off between (i) having many different colors (among which some with possibly low contrast and saturation) to resolve the ambiguity of emergences exceeding the tape-to-tape distance, and (ii) having only a few high-contrast, saturated colors to maximize the detectability of the tapes on the individual images.
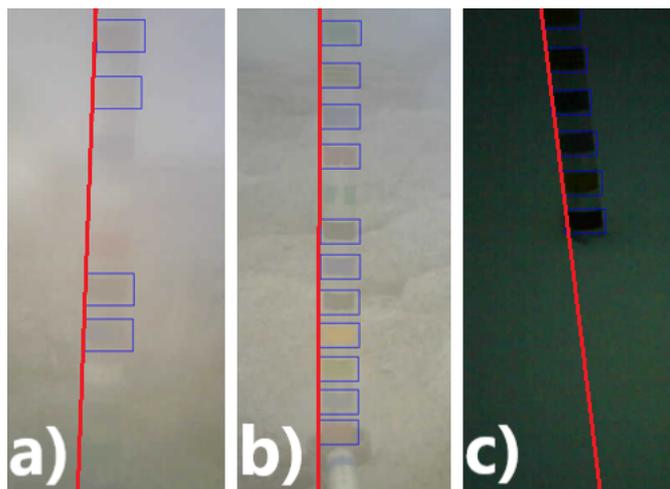
Figure 12. Template matching in challenging conditions: the algorithm proved to perform well and to detected many tapes even with fog (a, and b) and darkness (c).

5.4 Significance of heat waves

420 Because glacier melt that occurs during heat waves can be important for mitigating drought conditions ~~(Van Tiel et al., 2021; Ultee et al., 20~~ (Van Tiel et al., 2021; Pelto et al., 2022; Ultee et al., 2022), the individual heat waves are compared to each other. The first heat wave occurred in early summer (17-21 June 2022), and glacier melt is categorized as extreme in four out of five days (Fig. 9). The glacier storage change during this heat wave accounts for $0.30 \pm 0.05 \, \mathrm{km}^3$ w.e. Furthermore, the average daily glacier storage change during this heat wave is $4.96 \cdot 10^7 \, \mathrm{m}^3$ w.e d^{-1}, which is about three times higher than the average daily glacier

425 storage change of the past decade during the equivalent period. The second heat wave occurred between 14-26 July 2022, and glacier melt is categorized as extreme for nine out of thirteen days (Fig. 9). The average daily glacier storage change $(5.33 \cdot 10^7 \, \mathrm{m}^3$ w.e d$^{-1})$ is about twice as high as compared to the long-term average, and the total glacier storage change caused by this heat wave is $0.68 \pm 0.06 \, \mathrm{km}^3$ w.e. Even though the average daily glacier storage change has a similar magnitude for the June and the July heat waves ($4.96 \cdot 10^7 \, \mathrm{m}^3$ w.e d^{-1} and $5.33 \cdot 10^7 \, \mathrm{m}^3$ w.e d^{-1}, respectively), the difference between the

430 daily glacier storage change in 2022 and the decadal average is much higher for the June heat wave. This is because average melt is lower in June, thus making the June heat wave result more anomalous. Nevertheless, the July heat wave was more prolonged, thus causing larger absolute glacier mass loss. The third heat wave occurred between 31 July and 6 August, but during none of the seven days the melt was categorized as extreme (Fig. 9). The average daily glacier storage change, i.e. $4.05 \cdot 10^7 \, \text{m}^3 \, \text{w.e} \, \text{d}^{-1}$, is about the same as compared to the long-term average, and the amount of water produced during this

435 heat wave is $0.28 \pm 0.04 \, \text{km}^3$.

The definition of heat waves has an impact on this assessment, and other definitions – based on other temperature thresholds or on climatological temperature anomalies, for example – may be used. Even though, the chosen definition is simple, the threshold of 30 °C was used by a number of studies in Switzerland (Beniston, 2004; Beniston and Diaz, 2004) and Europe (Kovats et al., 2004; Hutter et al., 2007; Xu et al., 2016). In addition, we adopted the definition of Kyselỳ (2002) because the

440 minimum length of three days during which the temperature must be above 30 °C does not exclude short heat waves. For example, Kovats et al. (2004) used the same temperature threshold of 30 °C but a minimum number of six days during which the temperature must be above 30 °C, which would exclude the June heat wave that lasted five days.

The comparison of the three heat waves indicates that the July heat wave was the most severe. This is because of its long duration, causing about the same amount of glacier mass loss as the June and August heat waves combined. In terms of

445 magnitude, instead, the June and July heat waves are similar – the June heat wave being the most intense when compared to the long-term average melt. The comparison also proves the significance of melt occurring during heat waves for determining overall seasonal mass loss, as extreme heat events are expected to increase in the future (Fischer and Schär, 2010; Fischer et al., 2021). Furthermore, the large amounts of water that is produced during such short periods evidences the importance of monitoring short-term glacier mass balance variations. We suggest that this can be particularly important for optimizing the

450 use of glacier runoff for hydropower production, or for an adequate management of water supplies during heat and drought events (Zappa and Kan, 2007; Terrier et al., 2011; Anghileri et al., 2018; Landmann et al., 2021).

6 Conclusions

In this study, we developed a novel method for the automated derivation of daily glacier mass balance at the point scale. The method is based on computer-vision techniques which are used to read color-taped ablation stakes on time series of close-range

455 camera images. A daily mean absolute deviation of $0.81 \, \text{cm} \, \text{w.e} \, \text{d}^{-1}$ was found for the automated readings. By comparing the so-derived mass balance time series with the average mass balance of the past decade, we detected extreme melt events in the summer seasons of 2019-2022. A focus was set on summer 2022, which was extraordinary in terms of glacier melt rates. Three severe heat waves were identified, comprising a total of 23 melt events that we classify as extreme. This is about as many events as had occurred over the three previous years, emphasizing the exceptionality of the year. Our approach also detected 25

460 days of heat wave (i.e. days for which maximum air temperatures averaged over four reference station exceeded 30°C) during summer 2022, and demonstrated a high correlation between heat waves and extreme melt events. We assessed the glacier storage change that occurred at the scale of Switzerland and found that the 25 days of heat wave occurring during summer

2022 caused an amount of melt that, based on the average over the last decade, is equivalent to 56% of the melt expected for an entire summer. Despite the simplicity of the approach we use to upscale our point observations to the regional mass balance, we showed that extreme melt events occurring during heat days can be determinant for the total seasonal melt.

465

Our results evidence the importance of real-time observations for studying short-term mass balance variations, and provide a means for improving our understanding of the implications that a future climate – in which more frequent heat waves and extreme melt events are expected – will have on glacier runoff. By emphasizing the large amount of meltwater that is produced during short periods, the study confirms the role that glacier runoff has in attenuating the impacts of heat waves and drought events. We suggest that establishing systems for real-time monitoring of glacier mass balance and runoff could serve to optimize the use of meltwater for hydropower production, as well as to improve the management of water resources in a future, more extreme climate.

470

Code and data availability. The code of the automated algorithm, and the code used to process the data are available online at https://doi.org/10.5281/zenodo.7405281 (Cremona et al., 2023). Data is currently available at https://doi.org/10.3929/ethz-b-000602387

475

Video supplement. An example application of the automated ice ablation reading for station FIN 1 is available as a video under the following DOI: https://doi.org/10.5446/60100 (Cremona, 2022)

Author contributions. AC, MH, JML, and DF conceived the study. JB and AC developed the computer vision algorithm, with input from JML and DF. AC processed the images with the algorithm to derive the mass balance for 2019-2022. JML, MH, and AC made the visual readings of the image time series. AC wrote the manuscript and produced the figures, with contributions from all co-authors.

480

Competing interests. At least one of the (co-)authors is a member of the editorial board of The Cryosphere. The peer-review process was guided by an independent editor, and the authors have no other competing interests to declare.

Disclaimer. TEXT

Acknowledgements. This work was conducted in the frame of the project "Machine Learning aided ForecastIng of drought related eXtremes (MaLeFiX)", financed by the program "eXtremes" of the Swiss Federal Institute for Forest, Snow and Landscape Research WSL.

485 References

A2PS contributors: SmartStake: Monitor the glacier ablation with sub-hourly time step and millimetric accuracy, https://a2photonicsensors.com/smartstake-monitor-glacier-ablation/, last access on 13 December 2022, 2021.

Anghileri, D., Botter, M., Castelletti, A., Weigt, H., and Burlando, P.: A comparative assessment of the impact of climate change and energy policies on Alpine hydropower, Water Resources Research, 54, 9144–9161, https://doi.org/10.1029/2017WR022289, 2018.

490 Azam, M., Wagnon, P., Vincent, C., Ramanathan, A., Favier, V., Mandal, A., and Pottakkal, J.: Processes governing the mass balance of Chhota Shigri Glacier (western Himalaya, India) assessed by point-scale surface energy balance measurements, The Cryosphere, 8, 2195–2217, https://doi.org/10.5194/tc-8-2195-2014, 2014.

Bamber, J. L. and Rivera, A.: A review of remote sensing methods for glacier mass balance determination, Global and Planetary Change, 59, 138–148, https://doi.org/10.1016/j.gloplacha.2006.11.031, 2007.

495 Bauder, A., Matthias, H., Linsbauer, A., and (eds.): The Swiss Glaciers 2017/18 and 2018/19: Glaciological Report No. 139/140, https://doi.org/10.18752/glrep_139-140, 2020.

Beniston, M.: The 2003 heat wave in Europe: A shape of things to come? An analysis based on Swiss climatological data and model simulations, Geophysical Research Letters, 31, https://doi.org/10.1029/2003GL018857, 2004.

Beniston, M. and Diaz, H. F.: The 2003 heat wave as an example of summers in a greenhouse climate? Observations and climate model
500 simulations for Basel, Switzerland, Global and Planetary Change, 44, 73–81, https://doi.org/10.1016/j.gloplacha.2004.06.006, 2004.

Beraud, L., Cusicanqui, D., Rabatel, A., Brun, F., Vincent, C., and Six, D.: Glacier-wide seasonal and annual geodetic mass balances from Pléiades stereo images: application to the Glacier d'Argentière, French Alps, Journal of Glaciology, pp. 1–13, https://doi.org/10.1017/jog.2022.79, 2022.

Borner, J. and Cremona, A.: Determine real-time glacier mass changes from camera images [code documentation], https://rtgmc.readthedocs.
505 io/en/latest/index.html, 2020.

Bradski, G.: The OpenCV Library, Dr. Dobb's Journal of Software Tools, 2000.

Braithwaite, R. J.: Positive degree-day factors for ablation on the Greenland ice sheet studied by energy-balance modelling, Journal of Glaciology, 41, 153–160, https://doi.org/10.3189/S0022143000017846, 1995.

Carturan, L., Baroni, C., Brunetti, M., Carton, A., Dalla Fontana, G., Salvatore, M. C., Zanoner, T., and Zuecco, G.: Analysis of the mass
510 balance time series of glaciers in the Italian Alps, The Cryosphere, 10, 695–712, https://doi.org/10.5194/tc-10-695-2016, 2016.

Church, J. A., Gregory, J. M., Huybrechts, P., Kuhn, M., Lambeck, K., Nhuan, M. T., Qin, D., and Woodworth, P. L.: Changes in sea level, in: , in: JT Houghton, Y. Ding, DJ Griggs, M. Noguer, PJ Van der Linden, X. Dai, K. Maskell, and CA Johnson (eds.): Climate Change 2001: The Scientific Basis: Contribution of Working Group I to the Third Assessment Report of the Intergovernmental Panel, pp. 639–694, Cambridge University Press, 2001.

515 Cogley, J. G., Arendt, A., Bauder, A., Braithwaite, R., Hock, R., Jansson, P., Kaser, G., Moller, M., Nicholson, L., Rasmussen, L., et al.: Glossary of glacier mass balance and related terms, International Hydrological Programme, 2010.

Cremona, A.: Example application of the automated ice ablation reading on Findelgletscher, https://doi.org/10.5446/60100, 2022.

Cremona, A., Huss, M., Landmann, J. M., Borner, J., and Farinotti, D.: Heat wave contribution to 2022's extreme glacier melt from automated real-time ice ablation readings [code], https://doi.org/10.5281/zenodo.7405281, 2023.

520 Cullen, N. J., Mölg, T., Kaser, G., Steffen, K., and Hardy, D. R.: Energy-balance model validation on the top of Kilimanjaro, Tanzania, using eddy covariance data, Annals of Glaciology, 46, 227–233, https://doi.org/10.3189/172756407782871224, 2007.

Davaze, L., Rabatel, A., Dufour, A., Hugonnet, R., and Arnaud, Y.: Region-wide annual glacier surface mass balance for the European Alps from 2000 to 2016, Frontiers in Earth Science, 8, 149, https://doi.org/10.3389/feart.2020.00149, 2020.

Denzinger, F., Machguth, H., Barandun, M., Berthier, E., Girod, L., Kronenberg, M., Usubaliev, R., and Hoelzle, M.: Geodetic mass balance
525   of Abramov Glacier from 1975 to 2015, Journal of Glaciology, 67, 331–342, https://doi.org/10.1017/jog.2020.108, 2021.

Dussaillant, I., Berthier, E., and Brun, F.: Geodetic mass balance of the Northern Patagonian Icefield from 2000 to 2012 using two independent methods, Frontiers in Earth Science, 6, 8, https://doi.org/10.3389/feart.2018.00008, 2018.

Dyurgerov, M., Meier, M., and Armstrong, R. L.: Glacier mass balance and regime: data of measurements and analysis, vol. 55, Institute of Arctic and Alpine Research, University of Colorado Boulder, 2002.

530 Farinotti, D., Pistocchi, A., and Huss, M.: From dwindling ice to headwater lakes: could dams replace glaciers in the European Alps?, Environmental Research Letters, 11, 054 022, https://doi.org/10.1088/1748-9326/11/5/054022, 2016.

Fischer, E. M. and Schär, C.: Consistent geographical patterns of changes in high-impact European heatwaves, Nature Geoscience, 3, 398–403, https://doi.org/10.1038/ngeo866, 2010.

Fischer, E. M., Sippel, S., and Knutti, R.: Increasing probability of record-shattering climate extremes, Nature Climate Change, 11, 689–695,
535   https://doi.org/10.1038/s41558-021-01092-9, 2021.

Fischer, M., Huss, M., and Hoelzle, M.: Surface elevation and mass changes of all Swiss glaciers 1980-2010, The Cryosphere, 9, 525–540, https://doi.org/10.5194/tc-9-525-2015, 2015.

Fitzpatrick, N., Radić, V., and Menounos, B.: Surface energy balance closure and turbulent flux parameterization on a mid-latitude mountain glacier, Purcell Mountains, Canada, Frontiers in Earth Science, 5, 67, https://doi.org/10.3389/feart.2017.00067, 2017.

540 Fountain, A. G. and Vecchia, A.: How many stakes are required to measure the mass balance of a glacier?, Geografiska Annaler: Series A, Physical Geography, 81, 563–573, https://doi.org/10.1111/1468-0459.00084, 1999.

Friederichs, P.: Statistical downscaling of extreme precipitation events using extreme value theory, Extremes, 13, 109–132, https://doi.org/10.1007/s10687-010-0107-5, 2010.

Friederichs, P., Wahl, S., and Buschow, S.: Postprocessing for extreme events, in: Statistical Postprocessing of Ensemble Forecasts, pp.
545   127–154, Elsevier, https://doi.org/10.1016/B978-0-12-812372-0.00005-4, 2018.

Geibel, L., Huss, M., Kurzböck, C., Hodel, E., Bauder, A., and Farinotti, D.: Rescue and homogenization of 140 years of glacier mass balance data in Switzerland, Earth System Science Data, 14, 3293–3312, https://doi.org/10.5194/essd-14-3293-2022, 2022.

GLAMOS: Swiss Glacier Mass Balance, release 2021, Glacier Monitoring Switzerland, https://doi.org/10.18750/massbalance.2020.r2021, 2021.

550 GLAMOS: Swiss Glacier Mass Balance, release 2022, Glacier Monitoring Switzerland, https://doi.org/10.18750/massbalance.2022.r2022, 2022.

Grab, M., Mattea, E., Bauder, A., Huss, M., Rabenstein, L., Hodel, E., Linsbauer, A., Langhammer, L., Schmid, L., Church, G., Hellmann, S., Délèze, K., Schaer, P., Lathion, P., Farinotti, D., and Maurer, H.: Ice thickness distribution of all Swiss glaciers based on extended ground-penetrating radar data and glaciological modeling, Journal of Glaciology, 67, 1074–1092, https://doi.org/10.1017/jog.2021.55,
555   2021.

Gugerli, R., Salzmann, N., Huss, M., and Desilets, D.: Continuous and autonomous snow water equivalent measurements by a cosmic ray sensor on an alpine glacier, The Cryosphere, 13, 3413–3434, https://doi.org/10.5194/tc-13-3413-2019, 2019.

Hashemi, N. S., Aghdam, R. B., Ghiasi, A. S. B., and Fatemi, P.: Template matching advances and applications in image analysis, arXiv preprint arXiv:1610.07231, https://doi.org/10.48550/arXiv.1610.07231, 2016.

Hock, R.: Glacier melt: a review of processes and their modelling, Progress in Physical Geography, 29, 362–391, https://doi.org/10.1191/0309133305pp453ra, 2005.

Hock, R., Bliss, A., Marzeion, B., Giesen, R. H., Hirabayashi, Y., Huss, M., Radić, V., and Slangen, A. B.: GlacierMIP–A model intercomparison of global-scale glacier mass-balance models and projections, Journal of Glaciology, 65, 453–467, https://doi.org/10.1017/jog.2019.22, 2019.

Hugonnet, R., McNabb, R., Berthier, E., Menounos, B., Nuth, C., Girod, L., Farinotti, D., Huss, M., Dussaillant, I., Brun, F., et al.: Accelerated global glacier mass loss in the early twenty-first century, Nature, 592, 726–731, https://doi.org/10.1038/s41586-021-03436-z, 2021.

Huss, M.: Extrapolating glacier mass balance to the mountain-range scale: the European Alps 1900–2100, The Cryosphere, 6, 713–727, https://doi.org/10.5194/tc-6-713-2012, 2012.

Huss, M.: Density assumptions for converting geodetic glacier volume change to mass change, The Cryosphere, 7, 877–887, https://doi.org/10.5194/tc-7-877-2013, 2013.

Huss, M. and Bauder, A.: 20th-century climate change inferred from four long-term point observations of seasonal mass balance, Annals of Glaciology, 50, 207–214, https://doi.org/10.3189/172756409787769645, 2009.

Huss, M. and Hock, R.: Global-scale hydrological response to future glacier mass loss, Nature Climate Change, 8, 135–140, https://doi.org/10.1038/s41558-017-0049-x, 2018.

Huss, M., Bauder, A., Linsbauer, A., Gabbi, J., Kappenberger, G., Steinegger, U., and Farinotti, D.: More than a century of direct glacier mass-balance observations on Claridenfirn, Switzerland, Journal of Glaciology, 67, 697–713, https://doi.org/10.1017/jog.2021.22, 2021.

Hutter, H.-P., Moshammer, H., Wallner, P., Leitner, B., and Kundi, M.: Heatwaves in Vienna: effects on mortality, Wiener Klinische Wochenschrift, 119, 223–227, https://doi.org/10.1007/s00508-006-0742-7, 2007.

Immerzeel, W. W., Van Beek, L. P., and Bierkens, M. F.: Climate change will affect the Asian water towers, Science, 328, 1382–1385, https://doi.org/10.1126/science.1183188, 2010.

Immerzeel, W. W., Lutz, A., Andrade, M., Bahl, A., Biemans, H., Bolch, T., Hyde, S., Brumby, S., Davies, B., Elmore, A., et al.: Importance and vulnerability of the world's water towers, Nature, 577, 364–369, https://doi.org/10.1038/s41586-019-1822-y, 2020.

Klug, C., Bollmann, E., Galos, S. P., Nicholson, L., Prinz, R., Rieg, L., Sailer, R., Stötter, J., and Kaser, G.: Geodetic reanalysis of annual glaciological mass balances (2001–2011) of Hintereisferner, Austria, The Cryosphere, 12, 833–849, https://doi.org/10.5194/tc-12-833-2018, 2018.

Kovats, R. S., Hajat, S., and Wilkinson, P.: Contrasting patterns of mortality and hospital admissions during hot weather and heat waves in Greater London, UK, Occupational and Environmental Medicine, 61, 893–898, https://doi.org/10.1136/oem.2003.012047, 2004.

Kyselỳ, J.: Temporal fluctuations in heat waves at Prague–Klementinum, the Czech Republic, from 1901–97, and their relationships to atmospheric circulation, International Journal of Climatology: A Journal of the Royal Meteorological Society, 22, 33–50, https://doi.org/10.1002/joc.720, 2002.

Landmann, J. M., Künsch, H. R., Huss, M., Ogier, C., Kalisch, M., and Farinotti, D.: Assimilating near-real-time mass balance stake readings into a model ensemble using a particle filter, The Cryosphere, 15, 5017–5040, https://doi.org/10.5194/tc-15-5017-2021, 2021.

Linsbauer, A., Huss, M., Hodel, E., Bauder, A., Fischer, M., Weidmann, Y., Bärtschi, H., and Schmassmann, E.: The New Swiss Glacier Inventory SGI2016: from a topographical to a glaciological dataset, Frontiers in Earth Science, 9, 774, https://doi.org/10.3389/feart.2021.704189, 2021.

Lliboutry, L.: Multivariate Statistical Analysis of Glacier Annual Balances, Journal of Glaciology, 13, 371–392, https://doi.org/10.3189/S0022143000023169, 1974.

Lowe, D. G.: Distinctive image features from scale-invariant keypoints, International Journal of Computer Vision, 60, 91–110, https://doi.org/10.1023/B:VISI.0000029664.99615.94, 2004.

600 Marzeion, B., Hock, R., Anderson, B., Bliss, A., Champollion, N., Fujita, K., Huss, M., Immerzeel, W. W., Kraaijenbrink, P., Malles, J.-H., et al.: Partitioning the uncertainty of ensemble projections of global glacier mass change, Earth's Future, 8, e2019EF001470, https://doi.org/10.1029/2019EF001470, 2020.

Meteoswiss: Klimabulletin Jahr 2019, Tech. rep., Federal Office of Meteorology and Climatology, MeteoSwiss, 2020.

Mölg, N., Ceballos, J. L., Huggel, C., Micheletti, N., Rabatel, A., and Zemp, M.: Ten years of monthly mass balance of Conejeras glacier,
605 Colombia, and their evaluation using different interpolation methods, Geografiska Annaler: Series A, Physical Geography, 99, 155–176, https://doi.org/10.1080/04353676.2017.1297678, 2017.

Ohmura, A., Bauder, A., Müller, H., and Kappenberger, G.: Long-term change of mass balance and the role of radiation, Annals of Glaciology, 46, 367–374, https://doi.org/10.3189/172756407782871297, 2007.

O'Neel, S., McNeil, C., Sass, L. C., Florentine, C., Baker, E. H., Peitzsch, E., McGrath, D., Fountain, A. G., and Fagre, D.: Reanalysis of
610 the US Geological Survey Benchmark Glaciers: long-term insight into climate forcing of glacier mass balance, Journal of Glaciology, 65, 850–866, https://doi.org/10.1017/jog.2019.66, 2019.

OpenCV: OpenCV: template matching, https://docs.opencv.org/master/d4/dc6/tutorial_py_template_matching.html, last access on 20 October 2020, 2022.

Ostrem, G. and Stanley, A.: Glacier mass-balance measurements – A manual for field and office work, Department of Energy, Mines and
615 Resources, Ottawa, Ontario; Norwegian Water Resources and Electricity Board, Oslo, 1969.

Parkes, D. and Marzeion, B.: Twentieth-century contribution to sea-level rise from uncharted glaciers, Nature, 563, 551–554, https://doi.org/10.1038/s41586-018-0687-9, 2018.

Patro, E. R., De Michele, C., and Avanzi, F.: Future perspectives of run-of-the-river hydropower and the impact of glaciers' shrinkage: The case of Italian Alps, Applied Energy, 231, 699–713, https://doi.org/10.1016/j.apenergy.2018.09.063, 2018.

620 Pellicciotti, F., Brock, B., Strasser, U., Burlando, P., Funk, M., and Corripio, J.: An enhanced temperature-index glacier melt model including the shortwave radiation balance: development and testing for Haut Glacier d'Arolla, Switzerland, Journal of Glaciology, 51, 573–587, https://doi.org/10.3189/172756505781829124, 2005.

Pelto, M. S., Dryak, M., Pelto, J., Matthews, T., and Perry, L. B.: Contribution of glacier runoff during heat waves in the Nooksack river basin USA, Water, 14, 1145, https://doi.org/10.3390/w14071145, 2022.

625 Schaefli, B., Manso, P., Fischer, M., Huss, M., and Farinotti, D.: The role of glacier retreat for Swiss hydropower production, Renewable Energy, 132, 615–627, https://doi.org/10.1016/j.renene.2018.07.104, 2019.

Sold, L., Huss, M., Machguth, H., Joerg, P. C., Leysinger Vieli, G., Linsbauer, A., Salzmann, N., Zemp, M., and Hoelzle, M.: Mass balance re-analysis of Findelengletscher, Switzerland; benefits of extensive snow accumulation measurements, Frontiers in Earth Science, 4, 18, https://doi.org/10.3389/feart.2016.00018, 2016.

630 Stoffel, M. and Huggel, C.: Effects of climate change on mass movements in mountain environments, Progress in Physical Geography, 36, 421–439, https://doi.org/10.1177/0309133312441010, 2012.

Terrier, S., Jordan, F., Schleiss, A., Haeberli, W., Huggel, C., and Künzler, M.: Optimized and adapted hydropower management considering glacier shrinkage scenarios in the Swiss Alps, in: Proc. of International Symposium on Dams and Reservoirs under Changing Challenges, 79th Annual Meeting of ICOLD – Swiss Committee on Dams, pp. 497–508, CRC Press, Taylor & Francis Group, 2011.

635 Thibert, E., Eckert, N., and Vincent, C.: Climatic drivers of seasonal glacier mass balances: an analysis of 6 decades at Glacier de Sarennes (French Alps), The Cryosphere, 7, 47–66, https://doi.org/10.5194/tc-7-47-2013, 2013.

Thibert, E., Dkengne Sielenou, P., Vionnet, V., Eckert, N., and Vincent, C.: Causes of glacier melt extremes in the Alps since 1949, Geophysical Research Letters, 45, 817–825, https://doi.org/10.1002/2017GL076333, 2018.

Trewin, B., Cazenave, A., Howell, S., Huss, M., Isensee, K., Palmer, M. D., Tarasova, O., and Vermeulen, A.: Headline indicators for global
640 climate monitoring, Bulletin of the American Meteorological Society, 102, E20–E37, https://doi.org/10.1175/BAMS-D-19-0196.1, 2021.

Ultee, L., Coats, S., and Mackay, J.: Glacial runoff buffers droughts through the 21st century, Earth System Dynamics, 13, 935–959, https://doi.org/10.5194/esd-13-935-2022, 2022.

Van Tiel, M., Van Loon, A. F., Seibert, J., and Stahl, K.: Hydrological response to warm and dry weather: do glaciers compensate?, Hydrology and Earth System Sciences, 25, 3245–3265, https://doi.org/10.5194/hess-25-3245-2021, 2021.

645 Vincent, C., Fischer, A., Mayer, C., Bauder, A., Galos, S. P., Funk, M., Thibert, E., Six, D., Braun, L., and Huss, M.: Common climatic signal from glaciers in the European Alps over the last 50 years, Geophysical Research Letters, 44, 1376–1383, https://doi.org/10.1002/2016GL072094, 2017.

Vincent, C., Soruco, A., Azam, M., Basantes-Serrano, R., Jackson, M., Kjøllmoen, B., Thibert, E., Wagnon, P., Six, D., Rabatel, A., et al.: A nonlinear statistical model for extracting a climatic signal from glacier mass balance measurements, Journal of Geophysical Research:
650 Earth Surface, 123, 2228–2242, https://doi.org/10.1029/2018JF004702, 2018.

Vincent, C., Cusicanqui, D., Jourdain, B., Laarman, O., Six, D., Gilbert, A., Walpersdorf, A., Rabatel, A., Piard, L., Gimbert, F., et al.: Geodetic point surface mass balances: a new approach to determine point surface mass balances on glaciers from remote sensing measurements, The Cryosphere, 15, 1259–1276, https://doi.org/10.5194/tc-15-1259-2021, 2021.

Xu, Z., FitzGerald, G., Guo, Y., Jalaludin, B., and Tong, S.: Impact of heatwave on mortality under different heatwave definitions: a systematic
655 review and meta-analysis, Environment International, 89, 193–203, https://doi.org/10.1016/j.envint.2016.02.007, 2016.

Zappa, M. and Kan, C.: Extreme heat and runoff extremes in the Swiss Alps, Natural Hazards and Earth System Sciences, 7, 375–389, https://doi.org/10.5194/nhess-7-375-2007, 2007.

Zeller, L., McGrath, D., Sass, L., O'Neel, S., McNeil, C., and Baker, E.: Beyond glacier-wide mass balances: parsing seasonal elevation change into spatially resolved patterns of accumulation and ablation at Wolverine Glacier, Alaska, Journal of Glaciology, 69, 87–102,
660 https://doi.org/10.1017/jog.2022.46, 2022.

Zemp, M., Hoelzle, M., and Haeberli, W.: Six decades of glacier mass-balance observations: a review of the worldwide monitoring network, Annals of Glaciology, 50, 101–111, https://doi.org/10.3189/172756409787769591, 2009.

Zemp, M., Thibert, E., Huss, M., Stumm, D., Rolstad Denby, C., Nuth, C., Nussbaumer, S. U., Moholdt, G., Mercer, A., Mayer, C., et al.: Reanalysing glacier mass balance measurement series, The Cryosphere, 7, 1227–1245, https://doi.org/10.5194/tc-7-1227-2013, 2013.

665 Zemp, M., Frey, H., Gärtner-Roer, I., Nussbaumer, S. U., Hoelzle, M., Paul, F., Haeberli, W., Denzinger, F., Ahlstrøm, A. P., Anderson, B., et al.: Historically unprecedented global glacier decline in the early 21st century, Journal of Glaciology, 61, 745–762, https://doi.org/10.3189/2015JoG15J017, 2015.

Zemp, M., Huss, M., Thibert, E., Eckert, N., McNabb, R., Huber, J., Barandun, M., Machguth, H., Nussbaumer, S. U., Gärtner-Roer, I., et al.: Global glacier mass changes and their contributions to sea-level rise from 1961 to 2016, Nature, 568, 382–386,
670 https://doi.org/10.1038/s41586-019-1071-0, 2019.